Efficient Light-Emitting Diodes via Hydrogen Bonding Induced Phase Modulation in Quasi-2D Perovskites

*Lyuchao Zhuang, Qi Wei, Chuanzhao Li, Hui Ren, Yanyong Li, Fangyi Shi, Lingling Zhai, Kai Leng, Mingjie Li, Shu Ping Lau**

L.C. Zhuang, Dr. Q. Wei, Dr. C. Z. Li, H. Ren, Dr. Y. Y. Li, F. Y. Shi, Dr. L. L. Zhai, Dr. K. Leng, Dr. M. J. Li, Prof. S. P. Lau

Department of Applied Physics, Photonic Research Institute, The Hong Kong Polytechnic University

Hung Hom, Kowloon, Hong Kong, People's Republic of China

E-mail: apsplau@polyu.edu.hk

Keywords: phase modulation, anti-solvent, hydrogen bond, quasi-2D perovskite, light emitting diodes

Abstract

Quasi-2D perovskite has drawn considerable attention in light-emitting diodes due to their tunable energy landscape, efficient luminescence, and structural diversity. However, the excessive formation of low-n ($n \leq 2$) phases leads to lower carrier injection efficiency arising from the large injection barrier. Meanwhile, inefficient energy transfer caused by undesirable phases distribution result in multipeak emission. In this study, we use polar anti-solvent that can interact with spacer cations via strong hydrogen bonding, tailoring phases distribution to address the issue. The ethyl acetate treatment induces preferential growth of large-n phases and enhances energy transfer due to the strong hydrogen bonding energy ~ -17 kcal/mol. Leveraging these insights, we develop efficient sky-blue and green perovskite light-emitting diodes (PeLEDs) with improved external quantum efficiency (EQE) ranging from 4.21% to 8.77%. The anti-solvent treatment could open up a new avenue to regulate the phase distribution for an efficient energy funnel effect.

1. Introduction

Metal halide perovskites hold the potential for a new generation of light-emitting materials due to their unique properties such as tunable bandgap, solution processability, high defect tolerance, and narrow emission linewidth.[1-4] Tremendous progress has already been achieved in improving PeLEDs with different emitting colors based on three-dimensional (3D) perovskite films by tuning the composition of cations and/or halide anions.[5-9] The readily dissociated excitons stemming from inherent small exciton binding and long diffusion length lead to inefficient radiative recombination in 3D perovskites, resulting in luminescence quenching naturally.[10, 13]

Quasi-two-dimensional (quasi-2D) perovskites with strong quantum confinement offer an alternative approach for efficient PeLEDs.[14] Typically, the quasi-2D perovskites have a chemical formula of $L_2(APbBr_3)_{n-1}PbBr_4$, where L is a large organic spacer cation, A is a monovalent cation (e.g., Cs^+, methylammonium (MA^+) or formamidinium (FA^+)), and *n* represents the number of lead halide octahedral layers. Also, this unique multi quantum-well (QW) structure provides a funneling channel for photo- or electro-generated carriers and promotes radiative recombination.[15-17] However, due to the lower formation energy of small-*n* phases ($n \leq 2$), they are the phases in the films which are usually preferentially formed in solution-processed quasi-2D perovskite. A lower carrier injection efficiency arising from the large injection barrier between low n phase with high bandgap and electrode. These small-*n* phases broaden the bandgap of perovskite films and induce more lattice defects, resulting in inefficient energy transfer from small-*n* phases to large-*n* phases.[18-20] In other words,

the wide distribution of the low-*n* phases results in low emission efficiency and broad multiple electroluminescence (EL) peaks owing to the inefficient internal energy transfer.[21-23] Substantial efforts have been made in component and molecular engineering. For example, the synergistic effect of dual ligands to modulate the crystallization of quasi-2D perovskites was proposed, allowing the growth of intermediate-*n* phases to dominate.[19, 24-28] A self-assembling strategy with additive-assisted modulates low-dimensional phases.[10, 18, 29-32] The phase regulation strategies, most of which mainly focus on the composition, have been proven to enhance the performance of quasi-2D PeLEDs effectively. Recently, toluene anti-solvent treatment has been found to promote a fast nucleation rate and narrow the perovskite phase distribution.[29] Normally, the anti-solvent treatment has been widely employed during spin-coating to facilitate the removal of the host solvent(s), tuning the crystal nucleation and grain growth.[30] It has been recognized that anti-solvent treatment helps precipitate the perovskite crystals and suppress defects-induced nonradiative recombination.[31, 32] Nevertheless, a clear and systematic comparison of phase distribution for different anti-solvent treatments and an understanding these perovskite phases' crystallization kinetics is still lacking.

Herein, we explore differences in phase redistribution in perovskites treated with a series of anti-solvent, such as toluene (TO), diethyl ether (DE), chlorobenzene (CB), anisole (AN), and ethyl acetate (EA). We demonstrated that an EA treated approach facilitates energy transfer in the perovskite films for spectral stable PeLEDs. The strong hydrogen bonding between EA and organic cations effectively modulates the

crystallization kinetics and leads to $[PbBr_6]^{4-}$ cluster stacking growth. Furthermore, the energy cascade transfer can be dramatically boosted by optimizing the donor-acceptor ratio and desirable dimension distribution. Meanwhile, the EA-treated quasi-2D perovskite films can facilitate radiative recombination. The resulting PeLEDs achieve the maximum EQEs of 4.21%, 7.11%, and 8.77% for 490, 497, and 503 nm emissions, respectively. Furthermore, the fabricated sky-blue PeLEDs at 490 nm exhibit a half-lifetime (T_{50}) of 5.58 mins defined as the time when the device brightness declines to 50% of its initial value L_0 under a constant voltage of 4.5V. The EL spectra stay unchanged without any peak shift monitored during the entire stability test. Consequently, this work contributes to evolving approaches to realize highly performed and spectral stable PeLEDs.

2. Result and Discussion

The precursor solution of quasi-2D $PEA_2Cs_{n-1}Pb_nBr_{3n+1}$ (n = 3) perovskite was prepared by dissolving PEABr, CsBr and $PbBr_2$ in stoichiometric ratio. The dual ligand strategy has been proposed to achieve color-stable efficient PeLEDs based on the regulation of the ligand's confinement and coordination.[19, 24, 33, 34] Therefore, we introduced 80% BABr into the as-synthesized quasi-2D $PEA_2Cs_2Pb_3Br_{10}$ perovskite solution to form a BA^+ and PEA^+ mixed ligand system for easy demonstration. The ratio of x% BABr refers to the molar ratio between BABr and $PbBr_2$. During the spin-coating step, the TO, DE, CB, AN, and EA were used as anti-solvents to regulate the phase distribution in perovskites. The preparation details are discussed in the Methods.

In this work, perovskite films prepared without any anti-solvent are considered as the untreated samples.

Regarding the optical properties of perovskite films, Figure 1a shows UV-vis absorption spectra of the 80% BABr incorporated $PEA_2Cs_2Pb_3Br_{10}$ quasi-2D perovskite films untreated and treated with different anti-solvents. All the samples show distinct excitonic absorption peaks appearing at wavelengths of 428 nm and 454 nm corresponding to $n = 2$ and $n = 3$ phases in the quasi-2D perovskites.[25] However, for the perovskite films treated with AN and EA, we observed that the absorption peak of the $n = 2$ phase is significantly decreased, whereas the absorption peak of $n = 3$ phases is increased. Clearly, the change of excitonic absorption indicates the phase-modulation role happened in AN and EA anti-solvent treatments. The PL spectra in Figure 1b show that the untreated perovskite films exhibited an intense PL peak at 473 nm and two other peaks at 436 and 466 nm. The existence of a high fraction of low-n phases ($n \leq 3$) results in this phenomenon because of their relatively high exciton binding energy.[33, 34] In contrast, the emission peaks belonging to low-n phases become less identifiable for AN and EA-treated samples. The redshift of the PL peak may attribute to the recovery of the 3D nature of the emitting domains.[37] Therefore, the abovementioned results consistently show that nucleation restricts AN and EA's capability for low-n phases in quasi-2D perovskites, contributing to an efficient energy transfer.

Then, time-resolved photoluminescence (TRPL) measurement of these films was used to compare the trap passivation effect for anti-solvent treatment. The decay curves were fitted using a biexponential function, and detailed fitting parameters were

summarized in Table S1.[38] The EA-treated film exhibited the longest average lifetime (τ_{avg} = 11.26 ns) among these films. The inferior suppression of the low-*n* phases ($n \leq 2$) exerted by other anti-solvent results in a shortened lifetime because of their large exciton binding energy.[39] To further evaluate the effect of anti-solvent treatment on the electroluminescence (EL) properties, we fabricated the PeLEDs based on the device architecture of indium tin oxide (ITO)/ PEDOT:PSS / poly(9-vinylcarbazole) (PVK) / Perovskite / 1,3,5-tris(N-phenylbenzimidazol-2-yl) benzene (TPBi) / lithium fluoride (LiF)/ Al, as displayed in Figure S1. The device performance details were summarized in Table S2. Coincidently, we found that the PeLEDs using EA and AN treated (Figure 1e, f, and g) quasi-2D perovskite as an emissive layer show higher EQEs and sharper EL peaks compared to the untreated one. This trend is also well consistent with the PL results.

The reason why AN and EA anti-solvent treatments lead to a large redshift of the PL peaks and relative high-*n* phase distribution in quasi-2D perovskites, while TO, DE and CB treatments do not, is interesting. The physical properties of those anti-solvents are listed in Table S3. According to the relative polarity of CB and AN, we found the relative polarity of CB is 0.188 which is slightly lower than that of AN (0.198). However, the corresponding treated films differ significantly in their phase distribution. Solvents such as DE, AN, and EA all include oxygen-containing groups of atoms in their molecular structures. One is the carbonyl oxygen group and another is the ester group. In principle, the region with the largest electronegativity is located on the carbonyl oxygen atom, which provides the possibility of forming hydrogen-bonding

PEA^+ and BA^+ organic cations. Therefore, we suppose the intermolecular interaction between anti-solvent and organic cations will contribute to the phase distribution difference. We use the density functional theory (DFT) calculations to deeply uncover the effects of different anti-solvents at the molecular level. The nature of noncovalent interaction was studied using Independent Gradient Model (IGM) method.[40] The visualizations of IGM shown in Figure 1h confirm that EA molecule can provide hydrogen-bonding acceptor -O, forming hydrogen bonds C=O · · · N-H in the organic cations; here, N-H is a donor. DE, CB, and AN can all form hydrogen bonds with PEA^+ and BA^+ (Figure S2, S3, S4, Table S4, S5, S6). While, the hydrogen bonding energies of CB and AN are ~ -5 and -14 kcal/mol, respectively, which are weaker compared with EA (Figure S5, Table S7). The effects of different anti-solvents on the nucleation and growth of quasi-2D perovskite phases was illustrated in the scheme (Figure 1i). When the EA anti-solvent was adopted during the spin coating, the low-n phases will form at the initial stage due to the low formation energy as well as the poor solubility in the anti-solvent. However, the resident EA anti-solvent will foster the organic cations due to the strong hydrogen bonding. It will hinder the possibility of organic and $[PbBr_6]^{4-}$ combination. Therefore, the crystallization rate of intermedia phases slows, resulting in a large proportion of higher-n phases formation subsequently.[10-12] Although the DE can also form strong hydrogen bonding with the bonding energy around -17 kcal/mol with the organic cations, the low boiling point ~ 34.6 ℃ determines it can be readily volatile during the spin-coating process or the initial annealing stage. Thus, it can no longer serve as a modifier to regulate the phase distribution. ^1H nuclear magnetic

resonance (NMR) spectra were conducted to confirm the formation of hydrogen bonding (Figure S6). The proton resonance signal of ammonium (NH_3^+) of BA (peak at δ = 7.71 ppm) shifts to low-field after incorporation of EA anti-solvent (7.76 ppm). Similar changes were also found in the PEA and PEA-BA incorporated with EA mixture solutions. The variation in the chemical shift indicates the formation of hydrogen bonds between organic cations and EA anti-solvent, which leads to the de-shielding effect. [9, 10, 27, 41]

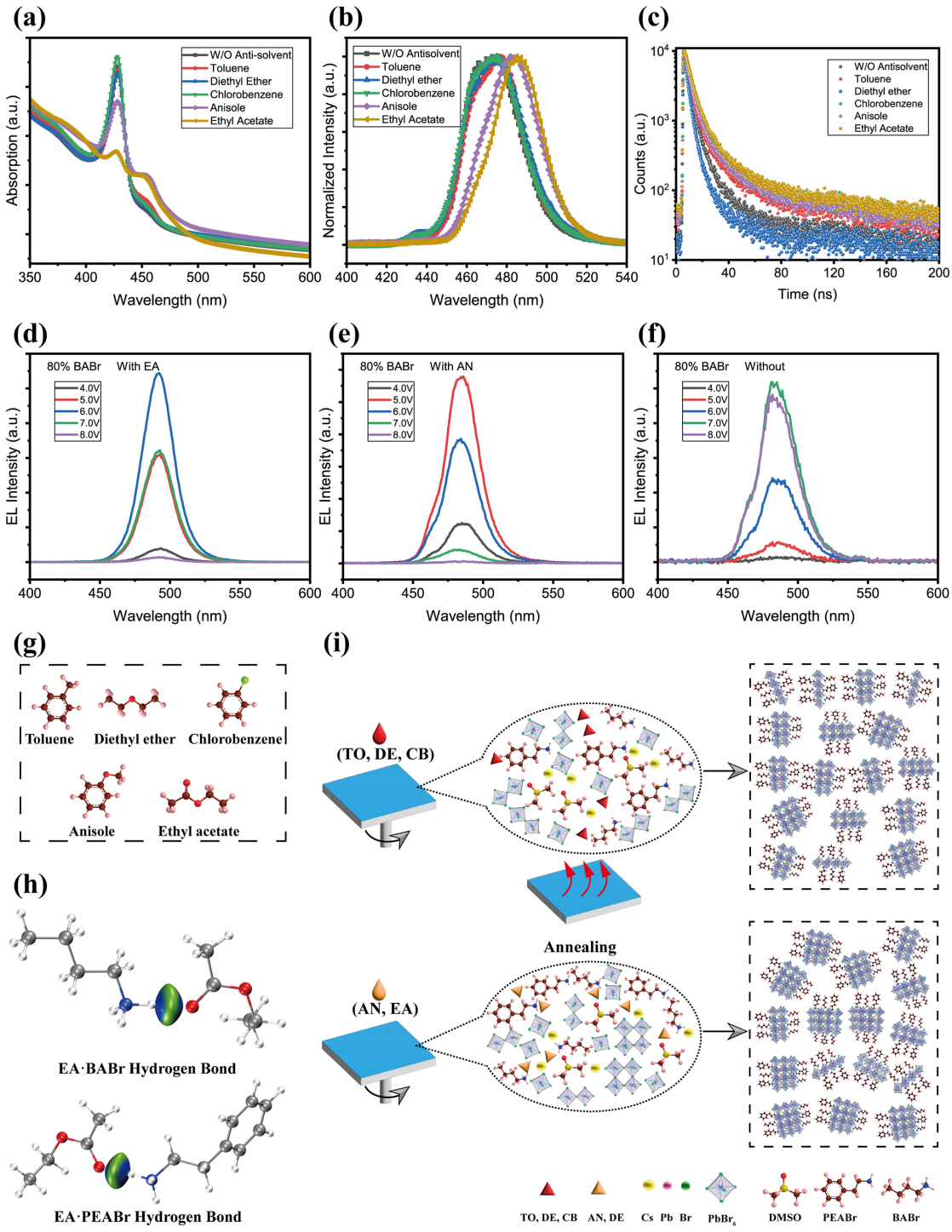

Figure 1. (a) UV-vis absorption (b) PL emission spectra (c) TRPL curves of the 80% BABr incorporated $PEA_2Cs_2Pb_3Br_{10}$ quasi-2D perovskite films with different anti-solvents treatment. EL spectra of (d) EA (e) AN and (f) un-treated 80% BABr incorporated $PEA_2Cs_2Pb_3Br_{10}$ quasi-2D perovskite film fabricated PeLEDs operating

under different voltages. (g) The chemical structure of different anti-solvents. (h) The schematics diagram of the hydrogen bonding between EA and organic cations. (i)The schematic diagram of the impacts of different anti-solvents on the nucleation and growth of quasi-2D perovskites.

As mentioned above, we found EA anti-solvent is the best modifier to regulate the high-*n* phase distribution and improve the EQE of the device compared to the other four anti-solvents. Then we comprehensively investigated the phase rearrangement for EA anti-solvent treatment for the BABr incorporated quasi-2D $PEA_2Cs_2Pb_3Br_{10}$ solution with the tunning ratio of BABr:$PbBr_2$. The normalized PL and UV-vis absorption spectra for untreated and EA treated perovskite films are displayed in Figures 2a, b. The addition of BABr progressively shifts the main PL emission from 500 to 437 nm as the BABr/$PbBr_2$ ratio increases from 40% to 120%. Also, the absorption peaks at ~ 454 nm (n = 3) gradually fade, whereas the absorption peaks at ~ 398 nm and ~ 428 nm increase (n = 1, 2) as the increase of BABr content. We attribute this feature to the fact that the incorporation of BA^+ cations is favorable to the formation of low *n* phases due to the high solubility of BABr.[34] Interestingly, as the EA anti-solvent treatment is adopted, the PL emission around 437 nm beloing to n = 2 is significantly suppressed (Figure 2a). Meanwhile, the PL spectra of the perovskite films exhibit redshift of the main emission compared with the untreated ones. By comparison, a significant decrease in the intensity of excitonic absorption peaks of low *n* phases is observed in the UV-vis spectra of EA-treated films.

TRPL was also measured to analyze the recombination process of the EA treated and untreated quasi-2D perovskite films with different amounts of BABr incorporated (Figure 2c). The PL decay time of the EA-treated perovskite is longer than that of the untreated one, indicating nonradiative recombination suppression (Table S8, S9). Moreover, compared with the untreated ones, fewer pinhole and dense films are observed in the SEM images for the EA-treated perovskites (Figure S7). Thus, we hypothesize that EA anti-solvent treatment helps mitigate defect formation in perovskite films, which is crucial for the corresponding PeLEDs.[42-44] To support this hypothesis, the defect density was evaluated for hole-only devices with the structures of ITO/PEDOT:PSS/perovskite/MoO_3/Al by performing space-charge-limited current (SCLC) measurements (Figure S8, S9). The device current is linearly proportional to the drive voltage up to the trap-filled limit (V_{TFL}). Therefore, it can be seen that the EA treated films show a lower V_{TFL} compared to those of the untreated ones, further confirming that the trap density in the perovskite films was reduced.

To further verify the change of phase distribution, the X-ray diffraction (XRD) pattern was performed to explore the structural property, as shown in Figures 2d, e, and S10. For the untreated films, the peaks at 2.9° and 15.3°, which can be assigned to the n = 3 and n = 2 phases, respectively. In contrast, the peak intensity related to the large-n phases (n = 3) gradually increases after EA treatment, while the n = 2 specie slowly fades out. Thus, the results unveil the evolution of the small-n (i.e., n = 2) phase to the larger-n phase (i.e., n = 3) in the different BABr amount incorporated-perovskite films

with the treatment of EA as further verified with the following transient absorption (TA) spectroscopy.

X-ray photoelectron spectroscopy (XPS) measurement of these films was then conducted to clarify the interactions of EA anti-solvent. The XPS spectra of Pb 4f are shown in Figure 2f, and the two peaks at 138.3 eV and 143.2 eV are attributed to Pb $4f_{7/2}$ and Pb $4f_{5/2}$ levels of Pb-Br, respectively. No drift is observed in the XPS spectra of Pb 4d after the treatment of EA, which further indicates that the EA treatment does not influence the internal structure of perovskite crystals. Moreover, after the EA anti-solvent treatment, the ratio of N/Pb decreases obviously (Figure 2g), which could be caused by the increase of higher-*n* phases.[37] This result agrees with the change of phase distribution by EA treatment. We also studied the effect of EA treatment on the perovskite morphology using atomic force microscopy (AFM) (Figure S10). The EA treated film's root-mean-square roughness (Rq) value is 1.96 nm, smaller than the untreated (2.56 nm). Also, the low surface roughness can facilitate contact with the electron-transport layer (ETL), thereby reducing interface resistance for accelerating charge transport.[45]

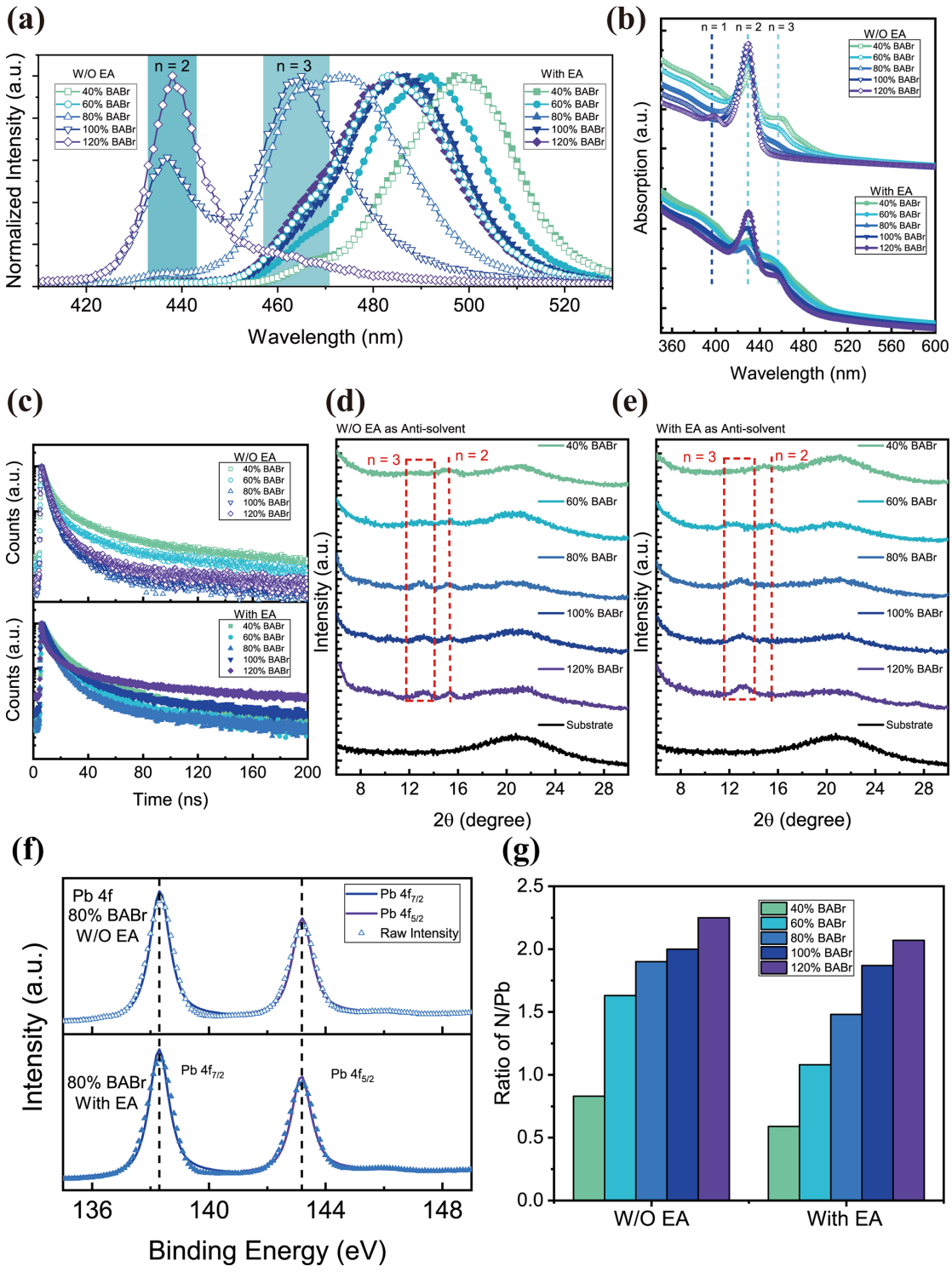

Figure 2. (a) PL spectra, (b) UV-vis absorption spectra, (c) TRPL decay curves and (d)(e) XRD patterns of w/o and with EA anti-solvent treated $PEA_2Cs_2Pb_3Br_{10}$ quasi-2D perovskite films with 40-120% BABr additives. (f) XPS spectra of Pb 4f and (g) N/Pb

ratios for as-synthesized quasi-2D perovskite films w/o and with EA anti-solvent treatment.

To investigate the dynamic details of recombination and transfer for photogenerated carriers, TA spectra measurement is carried out for the 80% BABr quasi-2D perovskite films with and without EA treatment. As shown in Figure 3a, three ground-state photobleaching (GSB, photoinduced absorption $\Delta A<0$) bands located at ~ 435 nm, ~ 465 nm, and ~ 487 nm can be distinguished, which originate from the $n = 2$, $n = 3$, and large-n ($n > 3$) phases in the untreated perovskite film. Their GSB intensities at 0.5 ps are depicted in Figure 3c, d to display the relative exciton contributions. Notably, the extracted phase distribution is dominated by $n = 2$ phase for the untreated perovskite film (Figure 3c). Furthermore, the intensity evolution of the GSB peaks corresponds to the evolution of excited-states populations in the corresponding phases.[16] The exciton resonance at $GSB_n = 2$ persists with a long delay time (10 ps), suggesting the incomplete energy transfer from excited excitons accumulated in the $n = 2$ phase to the lower n-phases.

On the contrary, a stronger GSB peak at around 465 nm is observed (Figure 3b, d), indicating the dominant $n = 3$ phase QWs exist in the EA-treated perovskite films. The kinetics of each GSB peak (Figure 3e, f) can be well-fitted by a multiexponential function with fitting parameters listed in Table S10. The fast decay components for $n = 2$ and $n = 3$ QWs bleaching are ascribed to the exciton energy transfer from low-n phases to the emitting phase ($n > 3$). While the slow decay component shall be due to complex decay processes such as trap-assisted recombination.[46] The fast decay

components with time constants (τ_1) of 0.55 ps (n = 2) and 0.40 ps (n = 3) match well with the lifetime (τ_{et}) of the rising component for $GSB_n > 3$, indicating the efficient and fast energy transfer to the large-n phase QWs. Consequently, these results confirm that the phases in our quasi-2D perovskites film are mixed, and the low-n phase can be efficiently suppressed by EA treatment. Also, the excitons funneled from the lower dimensional QWs eventually recombine in the $n > 3$ phases (Figure 3g). As discussed later, it is the main reason for the enhanced device performance.

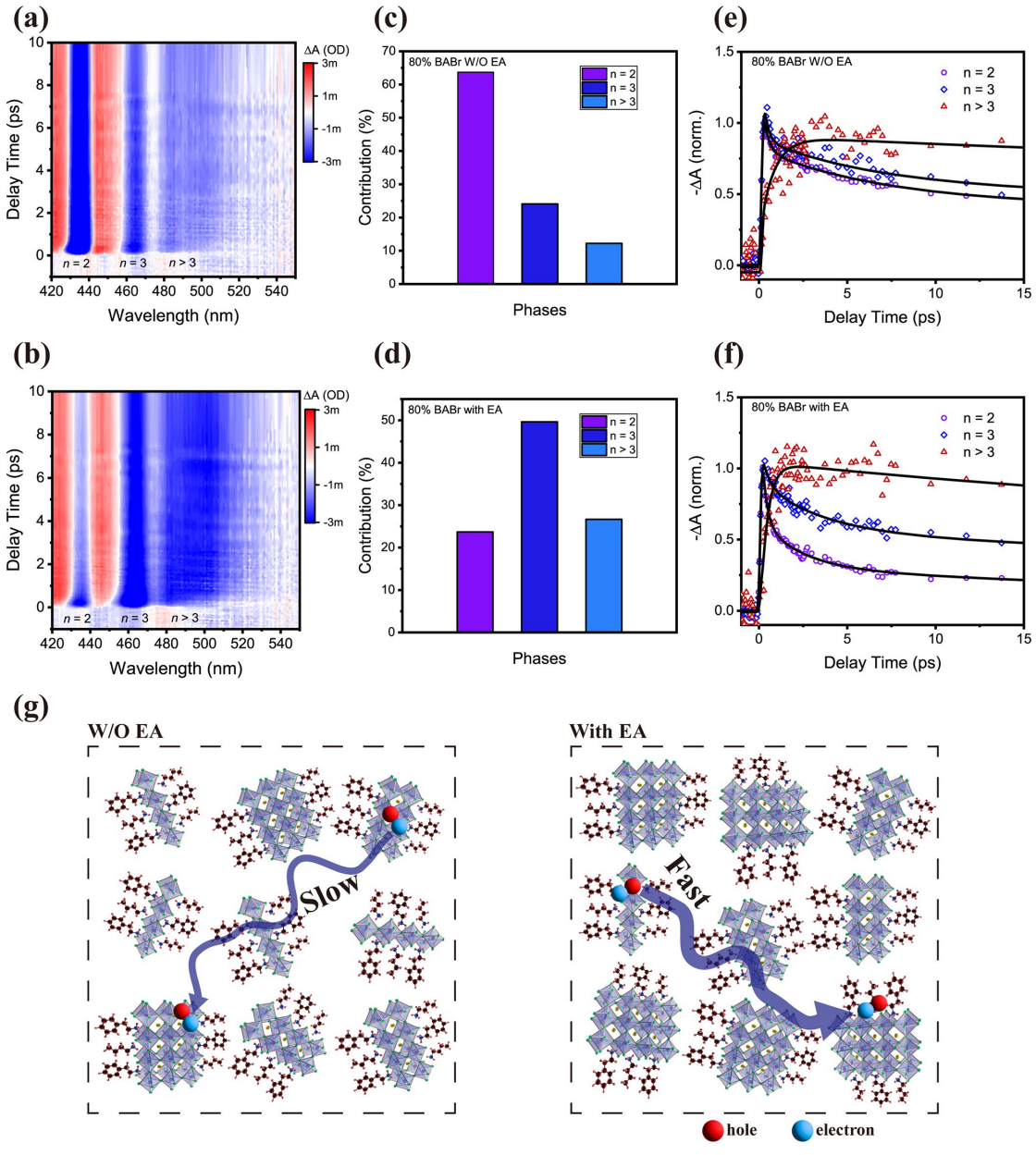

Figure 3. Controlling the energy landscape for quasi-2D perovskite film through EA anti-solvent treatment. (a)(b) Time–wavelength-dependent TA color maps. (c)(d) Exciton contributions from different phases according to intensity of GSB at 0.5 ps in TA spectra. (e)(f) TA kinetics traces probed at a different wavelength for the untreated (a, c, e) and EA treated perovskite films (b, d, f), respectively (excited at 400 nm). (g) Schematic diagrams demonstrating how the EA antisolvent influence the exciton energy transfer in the films.

Encouraged by the above studies, we fabricated the PeLEDs to investigate the phase redistribution effect of EA treatment on the EL properties of the quasi-2D perovskites. The device structure and corresponding energy alignment are shown in Figures 4a, and b, respectively. Luminescence (L) and current density (J) curves as a function of voltage (V), EQE-J curves for untreated and EA treated quasi-2D perovskite films based PeLEDs are shown in Figures 4c-f. The PeLEDs based on the untreated perovskite exhibit low performance and broad multiple EL peaks emission (Figure S11, Table S11). Compared with the EA treated quasi-2D perovskite films based PeLEDs, the current density of untreated one exhibit negligible difference which is expected to decrease as the BABr increases. For the untreated perovskite films, the formation of different phases and phase orientation are both uncontrollable. Thus, the electron/hole injection environment at the interface will be quite different. Whereas, for EA treated films, the main phase orientation will not change as BABr additive increases. Meanwhile, the proportion of large n phases used for light emission increased. Thus, the difference in the injection of electrons and holes would not be too great due to the

similar energy level. In addition, for this type I 2D/3D perovskite, charge carriers will funnel from small n phases through energy transfer to large n phases. Therefore, the main limitation of charge injection is still small n phases.

Meanwhile, the corresponding turn-on voltages are reduced from 3.6 V to 3.0 V for both the devices with 60% and 80% BABr after EA treatment, resulting from the improvement of energy level alignment because of the low-n phase suppression. Strikingly, the luminance for the EA treated devices are enhanced remarkably, yielding a maximum brightness of 3194.7, 1007.9, and 603.0 cd m^{-2} for the devices with 40%, 60%, and 80% BABr, respectively. In addition, the improved EQEs of 8.77%, 7.11%, and 4.21% of the corresponding devices are achieved. This enhancement is mainly attributed to suppressing the low-n phase induced efficient energy transfer. However, further increasing the BABr ratio to 100% and 120% exhibited inferior EQE and luminance (Figure S12). The introduction of a large amount of insulating organic spacing molecules in the film can disrupt and degrade the charge carrier transport and decrease radiative excitons in the emissive layers.[13] Moreover, an additional parasitic emission at 465 nm can be observed, which originates from the layered perovskite of n = 3, suggesting the deterioration of energy transfer.

The EA treated 80% BABr PeLEDs show a narrow band emission with the full width at half-maximum (FWHM) of around 27 nm and thus a good color purity with Commission Internationale de L'Eclairage (CIE) chromaticity coordinate at (0.071, 0.307) (Figure 4g). Also, the CIE coordinates of (0.048, 0.584) and (0.053, 0.451) are obtained for the 40% and 60% BABr PeLEDs, respectively. Furthermore, we recorded

the device stability of EA-treated and untreated 80% BABr films under continuous operation at a constant voltage of 4.5 V. The EA-treated sky-blue PeLEDs have a T_{50} of 5.58 mins at an initial luminance of 37 cd m^{-2}, which is six times longer than that of the untreated device (Figure 4h).

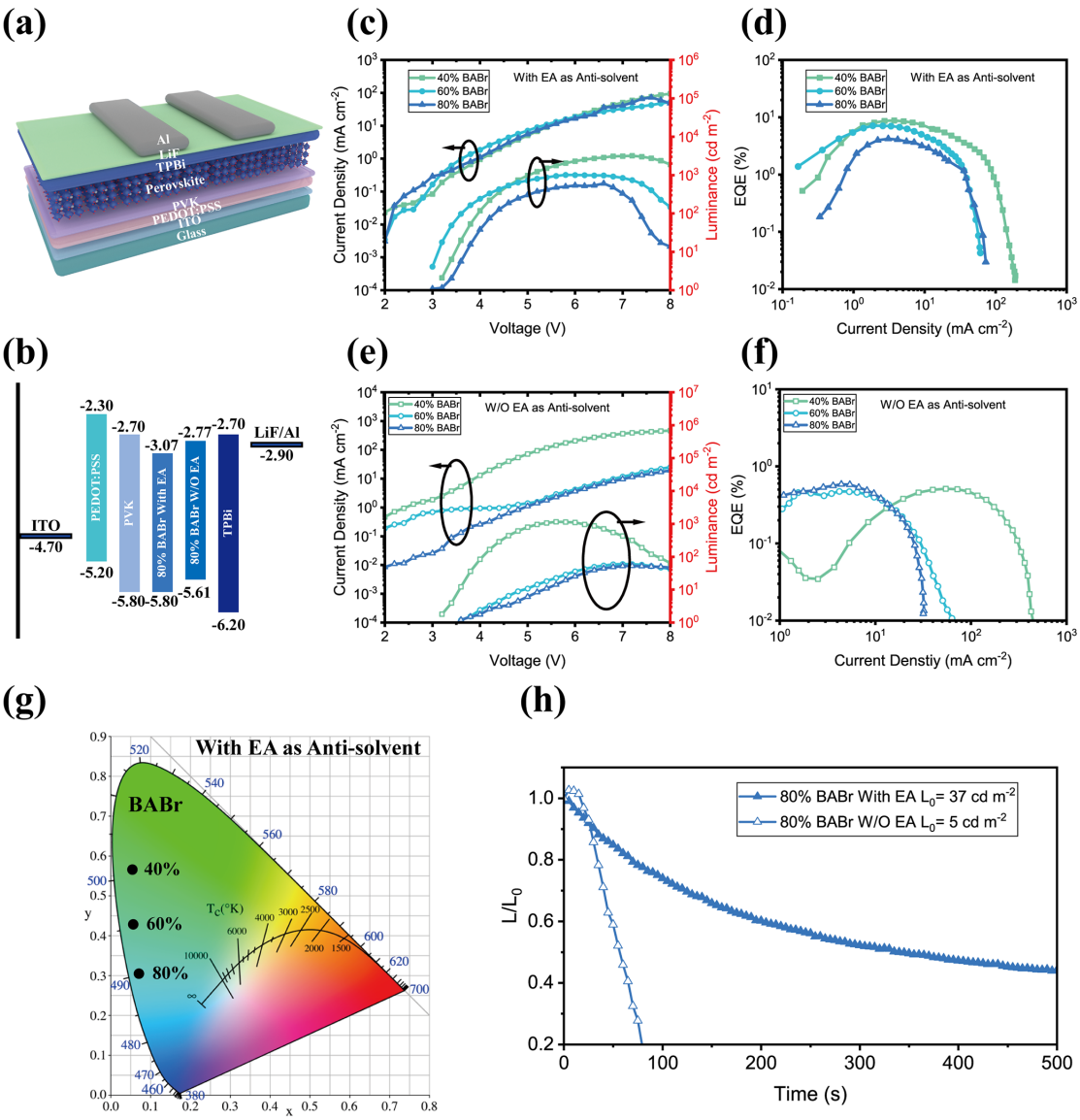

Figure 4. (a) Structure and (b) energy band alignment of the different layers of the fabricated PeLEDs. J-V-L and EQE-current density curves of the device based on various BABr with (c, d) and w/o EA (e, f) antisolvent treatment. (e) The CIE coordinates devices fabricated with various BABr%. (f) Operation lifetime of PeLEDs

devices with different initial luminance (L_0) (at a constant voltage of 4.5V, ambient condition, with encapsulation).

It is noteworthy that spectral stability is an important index to evaluate the PeLEDs performance. Finally, we compared the spectral stabilities of the EA treated (Figure 5a, b, c) and untreated (Figure 5d, e, f) quasi-2D perovskite films based PeLEDs under different operating voltages. It is found that only one single EL peak at the lowest energy belonging to the high-*n* perovskite phase is detected in the EA treated films with different BABr ratios, suggesting the highly efficient energy transfer from the low-*n* to large-*n* the phase in such EA-treated quasi-2D system. Also, the EL peak wavelength remains unchanged under different biases. Therefore, it implies that the EA anti-solvent treated PeLEDs have good spectral stability.

On the contrary, the untreated counterpart demonstrates an additional parasitic emission at 465 nm belonging to n = 3 phases and wider FWHMs, indicating the insufficient energy transfer between different phases. Moreover, even the emission 437 nm attributed n = 2 phase is observed from the broad multiple EL spectra for the high BABr ratio quasi-2D PeLEDs without EA treatment (Figure S11). Hence, the above comparison results demonstrated the superior phase distribution rearrangement ability and energy funneling effect facilitation for EA anti-solvent treatment.

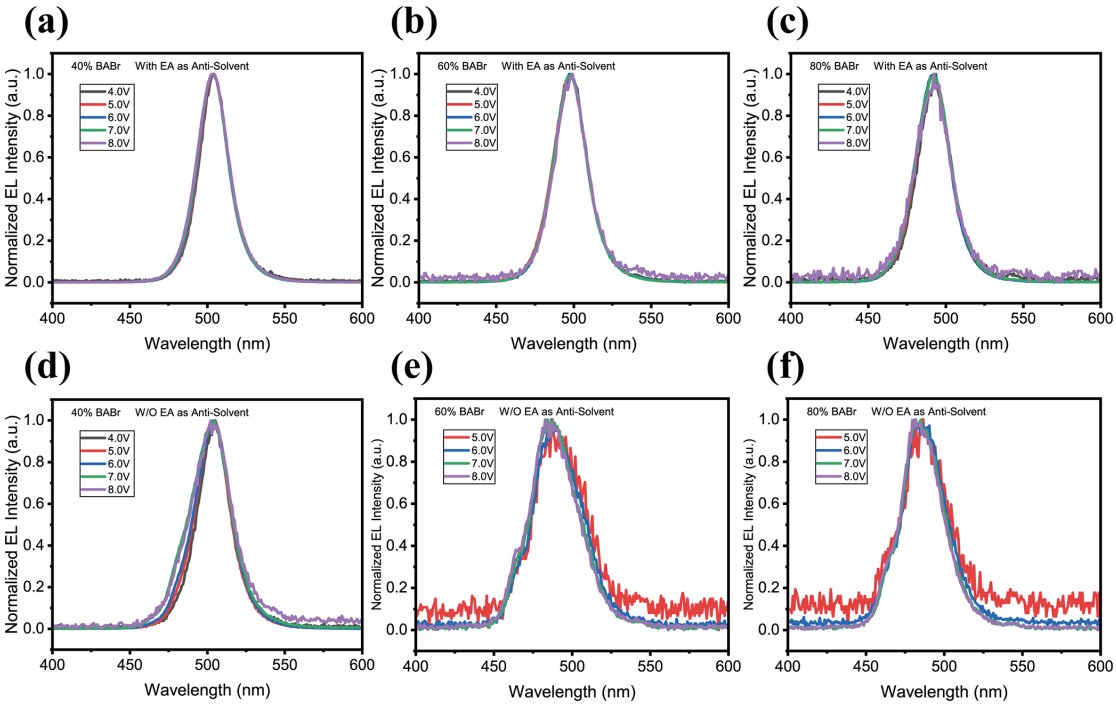

Figure 5. EL stability of PeLEDs based on the quasi-2D perovskite films with and w/o EA treated. EL spectra of (a, d) 40% BABr, (b, e) 60% BABr and (c, f) 80% BABr incorporated PeLEDs operating under different voltage.

3. Conclusion

In summary, we investigated the effects of TO, DE, CB, AN, and EA anti-solvent treatment on the crystallization process of different perovskite phases. We have demonstrated a unique strategy by EA treatment to decrease the low-*n* phases distribution in multiphases quasi-2D perovskite films. As a result, the proportion of higher-*n* phases with narrow bandgap has increased due to strong hydrogen bond between organic spacer cations and EA. The desirable phase distribution enables an efficient energy transfer process from donor to acceptor phases. Besides, the EA anti-solvent treatment can passivate the nonradiative defect, facilitating radiative recombination. Based on this synergistic effect, the maximum EQE of 4.21%, 7.11%, and 8.77% were obtained for PeLED with a stable emission peak at 490, 497, and 503 nm, respectively. Also, the fabricated EA treated sky-blue PeLEDs at 490 nm exhibit a T_{50} lifetime of 5.58 mins, which is six times that of the pristine one. This work provides a promising approach and inspiration for anti-solvent selection to modulate phase distribution for fabricating spectral stable and efficient PeLEDs.

4. Experimental Section

Materials: All chemicals used in this work are commercially available without further purification. CsBr (99.99%) and $PbBr_2$ (99.99%) were purchased from Xi'an Polymer Light Technology Corp. PEABr (99%) and BABr (99%) were purchased from Greatcell Solar Materials. TPBi, PVK (M_w= 20000), and LiF were purchased from Luminescence Technology Corp. Toluene, diethyl ether, chlorobenzene, anisole, ethyl acetate, and DMSO were purchased from Sigma-Aldrich.

Perovskite precursor solutions: The precursor solution of quasi-2D $PEA_2Cs_{n-1}Pb_nBr_{3n+1}$ (n = 3) perovskite was prepared by dissolving PEABr, CsBr, and $PbBr_2$ according to the molar ratio 2:2:3. And the concentration of Pb was kept at 0.2M. The ratio of x% BABr refers to the molar ratio between BABr and $PbBr_2$ (i.e., m_{BABr}/m_{PbBr2} = x%). The solution was stirred at 60℃ for overnight.

Fabrication of perovskite LED: Pattern ITO-coated glasses were ultrasonically cleaned with deionized water, acetone, and isopropyl alcohol for 15 mins each, and treated with Oxygen Plasma for 15 mins before depositing the PEDOT:PSS films. Afterward, the PEDOT:PSS was spin-coated on the substrate at 3000 rpm for 40 s, then annealing at 140℃ for 60 mins in air. Then, the substrates were transferred into an N_2-filled glovebox. PVK (6.0 mg ml^{-1} in chlorobenzene) was spin-coated at 4500rpm for 45s on the top of the PEDOT:PSS layer, annealing at 120℃ for 30mins. Next, the precursor solution was spin-coated onto the substrate via a one-step process at 4500 rpm for 60 s. For anti-solvent treated perpvskite films, the 150 ul of anti-solvent were poured onto the substrate after spin coating for 32s. During the spin coating process of the untreated

perovskite film, any anti-solvent will not be used. The resulting films were then annealed at 80 ℃ for 10 mins to remove the residual solvent. Finally, the device was completed by sequential vacuum deposition of TPBi, LiF, and Al under a high-vacuum atmosphere (<10^{-6} Torr). The thicknesses of TPBi, LiF, and Al are 40, 1, and 120 nm, respectively. The device area is 4.5 mm^2 by the overlapping area of the ITO and Al electrodes.

Characterization Measurement: Grazing incidence X-ray diffraction (GIXRD) analysis for the crystal structure was obtained by Cu Ka radiation (45 KV, 200 mA, Rigaku SmartLab 9kW), and the incident angle was 0.02°. The ultraviolet-visible absorbance spectra (UV-Abs) of the perovskite film were measured using a Perkin Elmer UV-vis-NIR spectrometer. The photoluminescence spectra (PL) were measured using an Edinburgh Photoluminescence FLS 920. Time-resolved photoluminescence (TRPL) was collected using time-correlated single-photon counting for 10000 counts. Excitation was provided by an Edinburgh EPL-375 nanosecond pulsed diode laser. The morphology was measured from field scanning electron microscopy (FESEM) images obtained from TESCAN MAIA3. X-ray photoelectron spectroscopy (XPS) and ultraviolet photoelectron spectroscopy (UPS) were measured on a Thermo Fisher Nexsa. The source was a monochromatic Al Kα (E_{photon} = 1486.6 eV) with a 10 mA filament current and a 12 keV filament voltage. XPS and UPS samples were prepared by spin-coating the perovskite precursor solution onto full ITO glass. UPS measurements utilized the He (I) photo line (21.22 eV) from a He discharge lamp, and the high-binding energy secondary electron cutoff (E_{cutoff}), and the HOMO region data were extracted

from the UPS spectra. The HOMO levels could be expressed as HOMO=21.22-(E_{cutoff}-E_{Δ}) (where E_{Δ} is the gap between the HOMO level and the Fermi level (E_F). The transient absorption (TA) measurements were performed on a femtosecond (fs) pump-probe system (Helios, Ultrafast System LLC) under ambient conditions. The pump pulses (wavelength: 400 nm, pump fluence: 0.2μJ cm^{-2} $pulse^{-1}$ at the sample surface, spot size: 2 mm) were generated by frequency doubling the 800 nm fs laser from a Ti: sapphire regenerative amplifier (Coherent Libra; 800 nm, 35 fs pulse width, 1 kHz) with a BBO crystal. The white-light probe continuum was generated by focusing the fundamental 800 nm beam from Ti: sapphire laser onto a sapphire plate (2 mm thick). The time delay between the pump and probe pulses was varied by a motorized optical delay line (maximum ≈8 ns).

PeLED characterization: A Keithley 2400 source-meter and a fiber integration sphere (FOIS-1) coupled with a QE Pro spectrometer (Ocean Optics) were utilized. The absolute radiance was calibrated by a standard Vis–NIR light source (HL-3P-INT-CAL plus, Ocean Optics). The EQE and spectral evolution with time was measured using the same system. All the measurements were conducted in an air ambience at room temperature and with encapsulation.

Supporting Information

Supporting Information is available from the Wiley Online Library or from the author.

Acknowledgements

This work was financially supported by the Hong Kong Polytechnic University grant (1-ZVGH).

Received: ((will be filled in by the editorial staff))

Revised: ((will be filled in by the editorial staff))

Published online: ((will be filled in by the editorial staff))

References

[1] Q. A. Akkerman, G. Rainò, M. V. Kovalenko, L. Manna, *Nat. Mater.* **2018**, 17, 394 - 405.

[2] J. H. Noh, S. H. Im, J. H. Heo, T. N. Mandal, S. I. Seok, *Nano Lett.* **2013**, 13, 1764 - 1769.

[3] T. Chiba, Y. Hayashi, H. Ebe, K. Hoshi, J. Sato, S. Sato, Y.-J. Pu, S. Ohisa, J. Kido, *Nat. Photonics* **2018**, 12, 681 - 687.

[4] H. Cho, S.-H. Jeong, M.-H. Park, Y.-H. Kim, C. Wolf, C.-L. Lee, J. H. Heo, A. Sadhanala, N. Myoung, S. Yoo, S. H. Im, R. H. Friend, T.-W. Lee, *Science* **2015**, 350, 1222 - 1225.

[5] L. Zhu, H. Cao, C. Xue, H. Zhang, M. Qin, J. Wang, K. Wen, Z. Fu, T. Jiang, L. Xu, Y. Zhang, Y. Cao, C. Tu, J. Zhang, D. Liu, G. Zhang, D. Kong, N. Fan, G. Li, C. Yi, Q. Peng, J. Chang, X. Lu, N. Wang, W. Huang, J. Wang, *Nat. Commun.* **2021**, 12, 5081.

[6] Y. Cao, N. Wang, H. Tian, J. Guo, Y. Wei, H. Chen, Y. Miao, W. Zou, K. Pan, Y. He, H. Cao, Y. Ke, M. Xu, Y. Wang, M. Yang, K. Du, Z. Fu, D. Kong, D. Dai, Y. Jin, G. Li, H. Li, Q. Peng, J. Wang, W. Huang, *Nature* **2018**, 562, 249 - 253.

[7] D.-H. Kang, S.-G. Kim, Y. C. Kim, I. T. Han, H. J. Jang, J. Y. Lee, N.-G. Park, *ACS Energy Lett.* **2020**, 5, 2191 - 2199.

[8] L. Zhao, K. M. Lee, K. Roh, S. U. Z. Khan, B. P. Rand, *Adv. Mater.* **2019**, 31, 1805836.

[9] W. Xu, Q. Hu, S. Bai, C. Bao, Y. Miao, Z. Yuan, T. Borzda, A. J. Barker, E.

Tyukalova, Z. Hu, M. Kawecki, H. Wang, Z. Yan, X. Liu, X. Shi, K. Uvdal, M. Fahlman, W. Zhang, M. Duchamp, J.-M. Liu, A. Petrozza, J. Wang, L.-M. Liu, W. Huang, F. Gao, *Nat. Photonics* **2019**, 13, 418 - 424.

[10] L. Kong, X. Zhang, Y. Li, H. Wang, Y. Jiang, S. Wang, M. You, C. Zhang, T. Zhang, S. V. Kershaw, W. Zheng, Y. Yang, Q. Lin, M. Yuan, A. L. Rogach, X. Yang, *Nat. Commun.* **2021**, 12, 1246.

[11] D. Zhang, Y. Fu, C. Liu, C. Zhao, X. Gao, J. Zhang, W. Guo, J. Liu, C. Qin, L. Wang, *Adv. Funct. Mater.* **2021**, 31, 2103890.

[12] X. Meng, J. Lin, X. Liu, X. He, Y. Wang, T. Noda, T. Wu, X. Yang, L. Han, *Adv. Mater.* **2019**, 31, 1903721.

[13] Z. Wang, F. Wang, W. Sun, R. Ni, S. Hu, J. Liu, B. Zhang, A. Alsaed, T. Hayat, Z. a. Tan, *Adv. Funct. Mater.* **2018**, 28, 1804187.

[14] Y. Jiang, J. Wei, M. Yuan, *J. Phys. Chem. Lett.* **2021**, 12, 2593 - 2606.

[15] M. Yuan, L. N. Quan, R. Comin, G. Walters, R. Sabatini, O. Voznyy, S. Hoogland, Y. Zhao, E. M. Beauregard, P. Kanjanaboos, Z. Lu, D. H. Kim, E. H. Sargent, *Nat. Nanotech.* **2016**, 11, 872 - 877.

[16] L. N. Quan, Y. Zhao, F. P. García de Arquer, R. Sabatini, G. Walters, O. Voznyy, R. Comin, Y. Li, J. Z. Fan, H. Tan, J. Pan, M. Yuan, O. M. Bakr, Z. Lu, D. H. Kim, E. H. Sargent, *Nano Lett.* **2017**, 17, 3701 - 3709.

[17] J. Byun, H. Cho, C. Wolf, M. Jang, A. Sadhanala, R. H. Friend, H. Yang, T.-W. Lee, *Adv. Mater.* **2016**, 28, 7515.

[18] Y. Tian, X.-Y. Qian, C.-C. Qin, M.-H. Cui, Y.-Q. Li, Y.-C. Ye, J.-K. Wang, W.-

J. Wang, J.-X. Tang, *Chem. Eng. J.* **2021**, 415, 129088.

[19] J. Xing, Y. Zhao, M. Askerka, L. N. Quan, X. Gong, W. Zhao, J. Zhao, H. Tan, G. Long, L. Gao, Z. Yang, O. Voznyy, J. Tang, Z.-H. Lu, Q. Xiong, E. H. Sargent, *Nat. Commun.***2018**, 9, 3541.

[20] L. N. Quan, M. Yuan, R. Comin, O. Voznyy, E. M. Beauregard, S. Hoogland, A. Buin, A. R. Kirmani, K. Zhao, A. Amassian, D. H. Kim, E. H. Sargent, *J. Am. Chem. Soc.* **2016**, 138, 2649 - 2655.

[21] S. Kumar, J. Jagielski, S. Yakunin, P. Rice, Y.-C. Chiu, M. Wang, G. Nedelcu, Y. Kim, S. Lin, E. J. G. Santos, M. V. Kovalenko, C.-J. Shih, *ACS Nano* **2016**, 10, 9720 - 9729.

[22] Q. Wang, J. Ren, X.-F. Peng, X.-X. Ji, X.-H. Yang, *ACS Appl. Mater. & Inter.* **2017**, 9, 29901 - 29906.

[23] Z. Chen, C. Zhang, X.-F. Jiang, M. Liu, R. Xia, T. Shi, D. Chen, Q. Xue, Y.-J. Zhao, S. Su, H.-L. Yip, Y. Cao, *Adv. Mater.* **2017**, 29, 1603157.

[24] Y. Jin, Z. K. Wang, S. Yuan, Q. Wang, C. Qin, K. L. Wang, C. Dong, M. Li, Y. Liu, L. S. Liao, *Adv. Funct. Mater.* **2019**, 30, 1908339.

[25] Z. Ren, L. Li, J. Yu, R. Ma, X. Xiao, R. Chen, K. Wang, X. W. Sun, W.-J. Yin, W. C. H. Choy, *ACS Energy Lett.* **2020**, 5, 2569 - 2579.

[26] T. L. Leung, H. W. Tam, F. Liu, J. Lin, A. M. C. Ng, W. K. Chan, W. Chen, Z. He, I. Lončarić, L. Grisanti, C. Ma, K. S. Wong, Y. S. Lau, F. Zhu, Ž. Skoko, J. Popović, A. B. Djurišić, *Adv. Optic. Mater.* **2020**, 8, 1901679.

[27] S. Yuan, Z.-K. Wang, L.-X. Xiao, C.-F. Zhang, S.-Y. Yang, B.-B. Chen, H.-T.

Ge, Q.-S. Tian, Y. Jin, L.-S. Liao, *Adv. Mater.* **2019**, 31, 1904319.

[28] F. Meng, X. Liu, Y. Chen, X. Cai, M. Li, T. Shi, Z. Chen, D. Chen, H.-L. Yip, C. Ramanan, P. W. M. Blom, S.-J. Su, *Adv. Funct. Mater.* **2020**, 30, 1910167.

[29] N. Yantara, N. F. Jamaludin, B. Febriansyah, D. Giovanni, A. Bruno, C. Soci, T. C. Sum, S. G. Mhaisalkar, N. Mathews, *ACS Energy Lett.* **2020**, 5, 1593 – 1600.

[30] N. J. Jeon, J. H. Noh, Y. C. Kim, W. S. Yang, S. Ryu, S. I. Seok, *Nat. Mater.* **2014**, 13, 897 - 903.

[31] W. Xu, Y. Gao, W. Ming, F. He, J. Li, X.-H. Zhu, F. Kang, J. Li, G. Wei, *Adv. Mater.* **2020**, 32, 2003965.

[32] Y. Huang, T. Liu, B. Wang, J. Li, D. Li, G. Wang, Q. Lian, A. Amini, S. Chen, C. Cheng, G. Xing, *Adv. Mater.* **2021**, 33, e2102816.

[33] S. Zeng, S. Shi, S. Wang, Y. Xiao, *J. Mater. Chem. C* **2020**, 8, 1319 - 1325.

[34] C. Wang, D. Han, J. Wang, Y. Yang, X. Liu, S. Huang, X. Zhang, S. Chang, K. Wu, H. Zhong, *Nat. Commun.* **2020**, 11, 6428.

[35] Z. Li, Z. Chen, Y. Yang, Q. Xue, H. L. Yip, Y. Cao, *Nat. Commun.* **2019**, 10, 1027.

[36] C.-H. Chen, Y.-H. Kuo, Y.-K. Lin, I. C. Ni, B.-H. Lin, C.-I. Wu, H.-L. Yip, C.-C. Kuo, C.-C. Chueh, *ACS Appl. Mater. & Inter.* **2022**, 14, 9587 – 9596.

[37] P. Pang, G. Jin, C. Liang, B. Wang, W. Xiang, D. Zhang, J. Xu, W. Hong, Z. Xiao, L. Wang, G. Xing, J. Chen, D. Ma, *ACS Nano* **2020**, 14, 11420 - 11430.

[38] C. Li, R. Zhu, J. Lai, J. Tan, Y. Luo, S. Ye, *J. Phys. Chem. Lett.* **2021**, 12, 11817.

[39] M. C. Gélvez-Rueda, M. B. Fridriksson, R. K. Dubey, W. F. Jager, W. van der

Stam, F. C. Grozema, *Nat. Commun.* 2020, 11, 1901.

[40] S. Emamian, T. Lu, H. Kruse, H. Emamian, *J. Comput. Chem.* **2019**, 40, 2868 - 2881.

[41] S. Shao, H. Duim, Q. Wang, B. Xu, J. Dong, S. Adjokatse, G. R. Blake, L. Protesescu, G. Portale, J. Hou, M. Saba, M. A. Loi, *ACS Energy Lett.* **2020**, 5, 39.

[42] W. Zhang, Y. Li, X. Liu, D. Tang, X. Li, X. Yuan, *Chem. Eng. J.* **2020**, 379, 122298.

[43] A. D. Taylor, Q. Sun, K. P. Goetz, Q. An, T. Schramm, Y. Hofstetter, M. Litterst, F. Paulus, Y. Vaynzof, *Nat. Commun.* **2021**, 12, 1878.

[44] J. Troughton, K. Hooper, T. M. Watson, *Nano Energy* **2017**, 39, 60 - 68.

[45] J. Carrillo, A. Guerrero, S. Rahimnejad, O. Almora, I. Zarazua, E. Mas-Marza, J. Bisquert, G. Garcia-Belmonte, *Adv. Energy Mater.* **2016**, 6, 1502246.

[46] G. Xing, B. Wu, X. Wu, M. Li, B. Du, Q. Wei, J. Guo, E. K. L. Yeow, T. C. Sum, W. Huang, *Nat. Commun.* **2017**, 8, 14558.

Entry for the Table of Contents

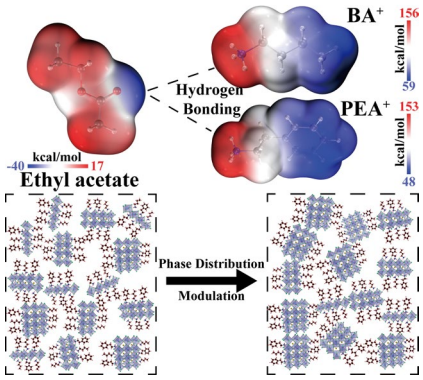

The low-n phase is commonly formed in solution-processed quasi-2D perovskite films due to the low formation energy, leading to the inefficient energy transfer. Anti-solvent treatment induced hydrogen bonding with organic spacer cations can modulate the crystallization kinetics and lead to $PbBr_6^{4-}$ cluster stacking growth.